

Phase separation of chemokinetic active particles

Euijoon Kwon,¹ Yongjae Oh,¹ and Yongjoo Baek^{1,*}

¹*Department of Physics and Astronomy & Center for Theoretical Physics,
Seoul National University, Seoul 08826, Republic of Korea*

(Dated: July 24, 2024)

Motility-induced phase separation (MIPS) is a well-studied nonequilibrium collective phenomenon observed in active particles. Recently, there has been growing interest in how coupling the self-propulsion of active particles to chemical degrees of freedom affects MIPS. Previous studies have shown that incorporating chemotaxis and the production or consumption of chemicals by active particles results in various pattern formations, such as arrested phase separation and traveling waves. In this study, we demonstrate that similar phenomena can be induced when active particles consume chemicals and exhibit chemokinesis, where higher chemical concentrations enhance self-propulsion without causing alignment with the chemical gradient. We discover that MIPS is intensified if chemical consumption is proportional to particle density but is suppressed if chemical consumption is closely tied to particle motion. This leads to a wider range of collective behaviors, including arrested phase separation and oscillating patterns. Our findings are based on a hydrodynamic theory derived from a particle-based model via standard methods.

I. INTRODUCTION

Active matter, or substances consisting of self-propelled units, has attracted much attention as a novel class of nonequilibrium systems exhibiting various collective phenomena [1–7]. Among these is the motility-induced phase separation (MIPS), which refers to the spontaneous separation between high- and low-density regions stemming from the self-propulsion and short-range repulsion of the particles [8–12]. To describe the phenomena, various theoretical frameworks have been developed, including top-down derivations of active field theories [13–15] and bottom-up derivations of coarse-grained hydrodynamic models [11, 16]. Predictions of these theories have also been tested by extensive numerics [17–20].

For simplicity, these studies have focused on active particles that propel themselves at constant speed and change directions only on their own accord. However, there have also been studies of how the coupling between active particles and chemicals affects the collective phenomena. They have particularly focused on *chemotaxis*, *i.e.*, the tendency of particles to move up (chemoattraction) or down (chemorepulsion) the chemical concentration gradient. If chemicals are produced by the particles themselves (autophoresis), it is known that both chemoattraction and chemorepulsion can induce phase separation [21, 22]. In particular, autophoresis with chemorepulsion leads to a variety of phase-separated patterns, such as dynamic clustering and traveling waves [23, 24]. Furthermore, when chemicals are injected into the system at a constant rate and chemoattractants are taken up by particles, then the MIPS can be arrested with dynamic instabilities [25]. These results indicate that the interplay between active particles and

chemicals can induce nontrivial changes in the collective behaviors.

On the other hand, even in the absence of chemotaxis, the chemical concentration may only affect the motility of active particles. This phenomenon, called *chemokinesis*, is found in various artificial and biological systems. For example, it is known that the velocity of a Pt-coated Janus particle increases with the local hydrogen peroxide concentration [26]. Another example is given by cilia and flagella of motile bacteria, whose beat frequency is strongly affected by the surrounding ATP concentration [27]. When such chemokinetic effects are combined with the inhomogeneous concentration fields caused by the chemical consumption of active particles, one can naturally expect the emergence of nontrivial clustering patterns.

To address this simple and practically relevant scenario, we explore a model system in which active particles are subject to both chemokinesis and chemical consumption. Through a hydrodynamic description of the system and linear stability analysis, we can analytically predict under which conditions the MIPS is enhanced or suppressed. We also observe microphase separation and oscillating patterns in our model, showing that chemokinetic effects are sufficient to induce a rich range of pattern formation behaviors.

The rest of the paper is organized as follows. In Sec. II, we introduce a model of chemical-consuming ABPs that exhibit chemokinesis, which is then coarse-grained to yield a hydrodynamic model. In Sec. III, we investigate phases and patterns generated by the hydrodynamic model, comparing predictions of the linear stability analysis with simulation results. In Sec. IV, the behaviors of the hydrodynamic model are compared with those of particle-based models. Finally, we summarize and conclude in Sec. V.

* y.baek@snu.ac.kr

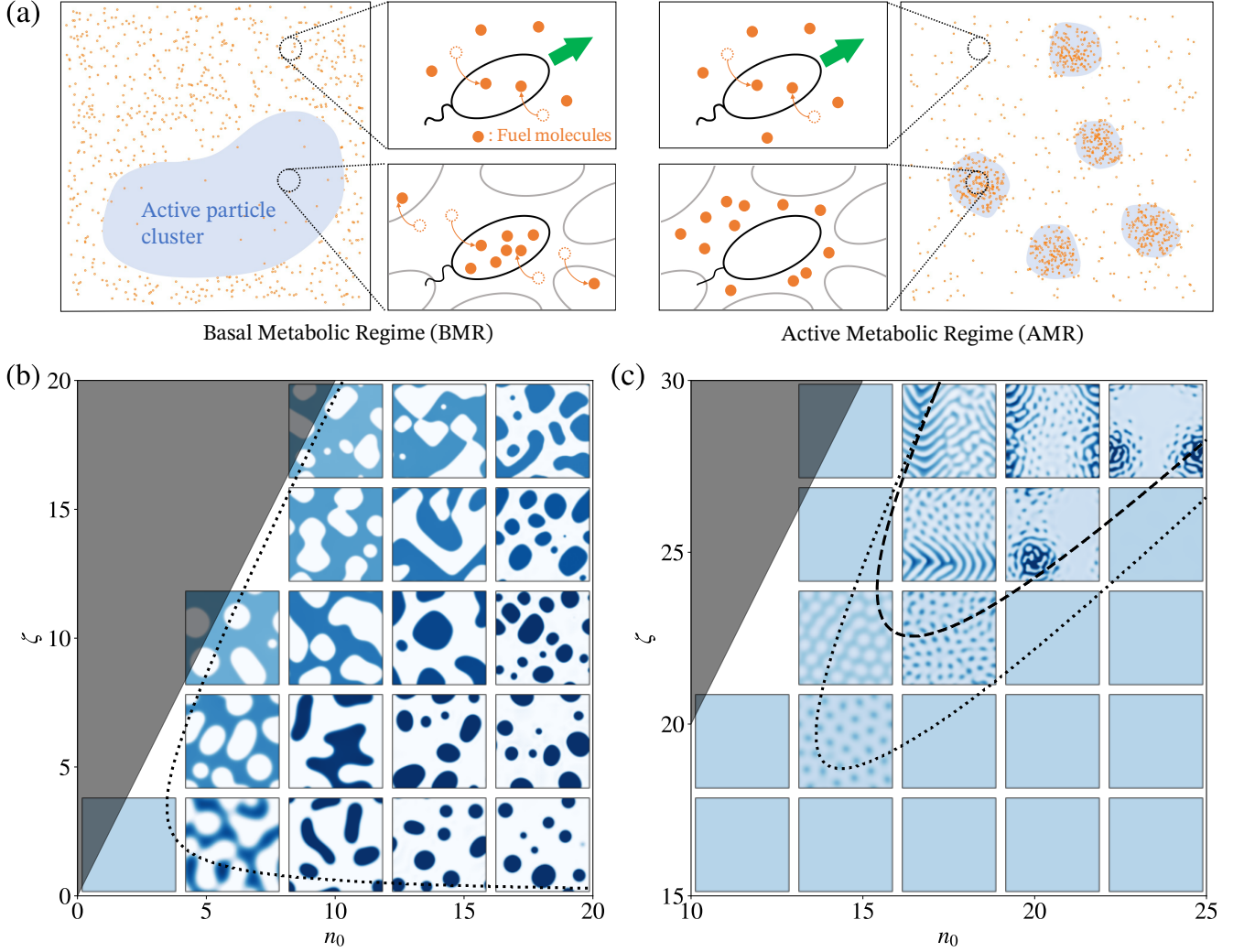


FIG. 1. (a) Schematic illustrations of two different regimes of local chemical consumption. Phase diagram of the hydrodynamic model in (b) the BMR with $\lambda = 0.01$, $D_c = 1$ and (c) the AMR with $\lambda = 0.5$, $D_c = 0.1$. The LSA predictions for the phase boundaries are indicated by the dotted (H-S boundary), the dash-dotted (H-O boundary), and the dashed (S-O boundary) lines. For comparison, snapshots of particle distribution (with darker regions indicating higher density) obtained by hydrodynamic simulations are shown together. The values of λ and D_c for each snapshot correspond to the coordinates of its center. The unphysical region with $v_{\text{eff}} < 0$ is grayed out. For this and all the other results in this paper, we use $\alpha = 1$, $\rho_0 = 0.5$, $D = 1$, $D_r = 3$, and $\kappa = 20$, unless mentioned otherwise.

II. MODEL

To formulate on a concrete basis how chemokinesis and chemical consumption affect the dynamics of active particles, we first introduce a particle-based model, from which a hydrodynamic theory can be derived by coarse-graining. More specifically, we consider N overdamped active Brownian particles (ABPs) moving within a two-dimensional chemical concentration profile $n(\mathbf{r}, t)$. The

equation of motion for each ABP is given by

$$\dot{\mathbf{r}}_k(t) = \mu \tilde{v}(n(\mathbf{r}_k, t)) \mathbf{e}_k - \sum_{k' \neq k} \mu \nabla_k V(|\mathbf{r}_k - \mathbf{r}_{k'}|) + \sqrt{2\mu T} \boldsymbol{\xi}_k, \quad (1)$$

where \mathbf{r}_k denotes the position of the k th ABP, μ the mobility of each ABP, \tilde{v} the magnitude of self-propulsion, \mathbf{e}_k the direction of self-propulsion exhibiting angular Brownian motion characterized by the rotational diffusion coefficient D_r , V the pairwise interaction between ABPs, T the temperature of the medium, and $\boldsymbol{\xi}_k$ a Gaussian white noise satisfying $\langle \boldsymbol{\xi}_k(t) \rangle = 0$ and $\langle \boldsymbol{\xi}_k(t) \boldsymbol{\xi}_{k'}(t') \rangle = \delta_{kk'} \mathbb{I} \delta(t - t')$ for the 2×2 identity matrix \mathbb{I} . Note

that chemokinesis is incorporated into the model via the dependence of \tilde{v} on the local chemical concentration $n(\mathbf{r}_k, t)$. Unlike chemotaxis, which aligns or anti-aligns \mathbf{e}_k to the concentration gradient, chemokinesis modifies only the motility of the active particle, as captured by the function $\tilde{v}(n)$. For simplicity, we focus on the linear regime where $\tilde{v}(n) = \alpha n$, with α controlling the strength of chemokinesis [28].

We also model how the chemical is consumed by active particles. To prevent the complete depletion of the chemical and keep the system out of equilibrium, we assume that the chemical is uniformly supplied into the system with a constant injection rate I . Then, the time evolution of the concentration profile can be written as

$$\dot{n}(\mathbf{r}, t) = D_c \nabla^2 n + I - \lambda f(n, \{\mathbf{r}_k, \dot{\mathbf{r}}_k\}), \quad (2)$$

where D_c is the diffusion constant of the chemical, λ is the consumption rate, and f is a function governing how the chemical consumption depends on the state of all ABPs and the chemical. The behaviors of f have been empirically studied for various species under different physical conditions [29, 30]. For simplicity, here we focus on two regimes of f that would differently affect the phase separation behavior of ABPs, as schematically illustrated in Fig. 1(a).

(i) *Basal Metabolic Regime* (BMR). In this case, the chemical is mostly used to maintain the routine metabolism of the ABPs, not their motion. Then the chemical consumption rate solely depends on how many ABPs are around, as expressed by

$$f(n, \{\mathbf{r}_k, \dot{\mathbf{r}}_k\}) = n(\mathbf{r}) \sum_{k'=1}^N \delta(\mathbf{r} - \mathbf{r}_{k'}) . \quad (3)$$

In the BMR, the chemical consumption rate increases with the density of ABPs, which would lower the chemical concentration within ABP clusters. The resulting chemokinetic slowdown hinders the ABPs from escaping the cluster. Thus, one can naturally expect that the phase-separating tendencies are strengthened in the BMR.

(ii) *Active Metabolic Regime* (AMR). In this regime, the chemical is mostly used when the ABPs actually move. Then the chemical consumption rate depends on how quickly the ABPs move in the self-propulsion direction, as expressed by

$$f(n, \{\mathbf{r}_k, \dot{\mathbf{r}}_k\}) = n(\mathbf{r}) \sum_{k'=1}^N \dot{\mathbf{r}}_{k'} \cdot \mathbf{e}_{k'} \delta(\mathbf{r} - \mathbf{r}_{k'}) . \quad (4)$$

In the AMR, the chemical consumption rate drops if the ABPs are stuck together, resulting in the accumulation of chemical within the ABP clusters. Then the ensuing chemokinetic speedup makes the cluster more prone to disintegration. Thus, in contrast to the BMR, one can expect that the phase-separating tendencies are weakened in the AMR.

The particle-based model described thus far can be coarse-grained following the standard procedure given in Ref. [11]. This yields a system of hydrodynamic equations in terms of the particle density $\rho(\mathbf{r}, t)$ and the chemical concentration $n(\mathbf{r}, t)$, as shown below:

$$\begin{aligned} \dot{\rho}(\mathbf{r}, t) &= \nabla \cdot \left\{ D \nabla \rho + \frac{v(\rho, n)}{2D_r} \nabla [v(\rho, n)\rho] - \kappa \nabla (\nabla^2 \rho) \right\} , \\ \dot{n}(\mathbf{r}, t) &= D_c \nabla^2 n + I - \begin{cases} \lambda \rho n & \text{(BMR)} \\ \lambda \rho v(\rho, n) n & \text{(AMR)} \end{cases} . \end{aligned} \quad (5)$$

Here D is the ABP diffusion coefficient, κ is a parameter setting the interfacial energy, and $v(\rho, n)$ is the effective self-propulsion strength accounting for both acceleration by chemokinesis and deceleration by interparticle repulsion. Through the rest of the study, we focus on the linear regime where

$$v(\rho, n) = \alpha n - \rho \zeta , \quad (6)$$

so that the positive coefficient ζ quantifies the slowdown effect. We propose this hydrodynamic model, expressed by Eqs. (5) and (6), as a minimal model for exploring the effects of chemokinesis and chemical consumption on the MIPS, which is discussed in the next section.

III. LINEAR STABILITY ANALYSIS AND HYDRODYNAMIC SIMULATION

In this section, we investigate various phases of the hydrodynamic model expressed by Eqs. (5) and (6). Towards this end, we first conduct linear stability analysis (LSA) to predict when and how homogeneous solutions become unstable. Then, the analytical results are compared with numerical simulations of the hydrodynamic model.

Before moving on to the details, let us give a brief sketch of how LSA is done. The homogeneous density and concentration profiles $\rho(\mathbf{r}, t) = \rho_0$ and $n(\mathbf{r}, t) = n_0$ can solve Eq. (5) when the injection rate is given by

$$I = \begin{cases} \lambda \rho_0 n_0 & \text{(BMR)} \\ \lambda \rho_0 v(\rho_0, n_0) n_0 & \text{(AMR)} \end{cases} . \quad (7)$$

Assuming this condition, we let the density and the concentration profiles fluctuate by $\delta\rho(\mathbf{r}, t)$ and $\delta n(\mathbf{r}, t)$, respectively. Taking the Ansatz $\delta\rho = \delta\rho_0 e^{i\mathbf{q}\cdot\mathbf{r} + \omega t}$ and $\delta n = \delta n_0 e^{i\mathbf{q}\cdot\mathbf{r} + \omega t}$, Eq. (5) can be linearized as an eigenvalue equation

$$\begin{pmatrix} \mathcal{A} & \mathcal{B} \\ \mathcal{C} & \mathcal{D} \end{pmatrix} \begin{pmatrix} \delta\rho_0 \\ \delta n_0 \end{pmatrix} = \omega \begin{pmatrix} \delta\rho_0 \\ \delta n_0 \end{pmatrix} . \quad (8)$$

See Appendix A for explicit expressions of the matrix elements \mathcal{A} , \mathcal{B} , \mathcal{C} , and \mathcal{D} . The eigenvalue ω thus satisfies

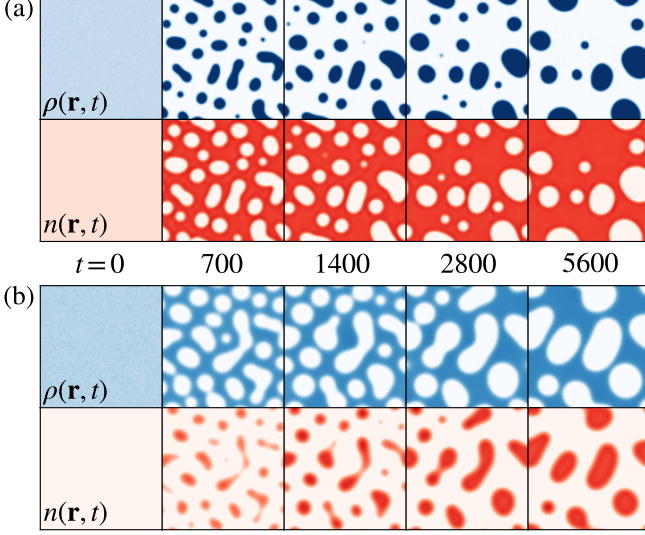


FIG. 2. Evolution of particle density $\rho(\mathbf{r}, t)$ and chemical concentration $n(\mathbf{r}, t)$ in the hydrodynamic simulation of the BMR for (a) $n_0 = 18$, $\zeta = 6$ and (b) $n_0 = 6$, $\zeta = 6$. The other parameters are identical to those used in Fig. 1(b).

the characteristic equation $\omega^2 - (\mathcal{A} + \mathcal{D})\omega + \mathcal{A}\mathcal{D} - \mathcal{B}\mathcal{C} = 0$, whose roots are given by

$$\omega_{\pm} = \frac{1}{2} \left[\mathcal{A} + \mathcal{D} \pm \sqrt{(\mathcal{A} - \mathcal{D})^2 + 4\mathcal{B}\mathcal{C}} \right]. \quad (9)$$

Depending on how the real and the imaginary parts of ω_{\pm} vary with $q^2 \equiv \mathbf{q} \cdot \mathbf{q}$, we can identify three phases. First, when $\text{Re} \omega_{\pm} < 0$ for all q^2 , the homogeneous profiles are stable against fluctuations, resulting in the homogeneous (H) phase. Second, if $\text{Re} \omega_{\pm} > 0$ for some interval of q^2 and $\text{Im} \omega_{\pm} = 0$ there, then any slight deviations from the homogeneous profiles would grow exponentially until the LSA breaks down. Assuming that the lack of oscillation persists beyond the LSA regime, this behavior would result in a coexistence phase where high-density and low-density regions form a largely stable interface, which we call the stationary (S) phase. Finally, when there is an interval of q^2 with $\text{Re} \omega_{\pm} > 0$ and $\text{Im} \omega_{\pm} \neq 0$, perturbations of the homogeneous profiles exhibit oscillations with growing amplitudes. We call this regime the oscillatory (O) phase.

While we have defined these three phases in terms of the behaviors of the system in the LSA regime, the true steady-state behaviors, which may lie well beyond the LSA regime, can be different. In the following, we separately discuss the LSA predictions of the three phases for the BMR and the AMR, which are then compared with numerics.

A. BMR facilitates phase separation

For the BMR, one can easily check that $\mathcal{B}\mathcal{C} > 0$ for all q^2 as long as $v_0 \equiv \alpha n_0 - \rho_0 \zeta > 0$, which must be true in the regime where Eq. (6) is a good approximation. Thus, the BMR lacks the O phase, and we only need to consider the boundary between the H and the S phases. As detailed in Appendix A, the boundary is derived as

$$D_{\text{BMR}} = \frac{\rho_0 \zeta (\alpha n_0 - \rho_0 \zeta)}{D_r}, \quad (10)$$

so that $D > D_{\text{BMR}}$ ($D < D_{\text{BMR}}$) corresponds to the H phase (S phase). Interestingly, D_{BMR} does not depend on the value of the chemical consumption rate λ , marking the onset of MIPS whenever $\lambda > 0$.

When $\lambda = 0$, there is no chemical consumption, so $n(\mathbf{r}, t)$ stays at its initial value n_0 . Since the chemical concentration does not change anywhere, the effective self-propulsion strength can be written as $v(\rho, n) = v_0 - \rho \zeta$, where $v_0 \equiv \alpha n_0$ is a fixed constant. In this case, chemokinesis becomes completely irrelevant, effectively reducing the dynamics of the system to those of the *vanilla* model decoupled from the chemicals. Then, as detailed in Appendix A, the phase boundary is determined by the effective diffusion coefficient

$$D_{\text{eff}} \equiv D + \frac{(v_0 - \rho_0 \zeta)(v_0 - 2\rho_0 \zeta)}{2D_r} \quad (11)$$

that governs the collective relaxation of density profiles when only the short-range repulsion between particles is taken into account (via ζ). The MIPS occurs when and only when $D_{\text{eff}} < 0$, which yields the phase boundary

$$D_{\text{vanilla}} = \frac{(\alpha n_0 - \rho_0 \zeta)(2\rho_0 \zeta - \alpha n_0)}{2D_r} \quad (12)$$

so that $D > D_{\text{vanilla}}$ ($D < D_{\text{vanilla}}$) corresponds to the H phase (S phase). Comparing the above formula with Eq. (10), it is clear that $D_{\text{BMR}} > D_{\text{vanilla}}$ always holds, indicating that nonzero λ broadens the S phase at the expense of the H phase. Thus, as previously expected, the BMR facilitates MIPS.

It is notable that the phase boundary changes discontinuously from D_{vanilla} to D_{BMR} as the chemical consumption is turned on. When the chemicals are irrelevant, MIPS occurs only via the deceleration of particles with increasing density. In contrast, when $\lambda > 0$, high local particle density and low local chemical concentration can support each other via positive feedback, creating density and concentration modulations against diffusive currents. When the particle-chemical coupling λ is small, the density-concentration feedback can overcome only small diffusion currents, which means that only long-wavelength modulations can be maintained. Nonetheless, whenever $\lambda > 0$, there exists a finite wavelength above which the density and concentration modulations can be amplified against diffusive currents. Thus, the mecha-

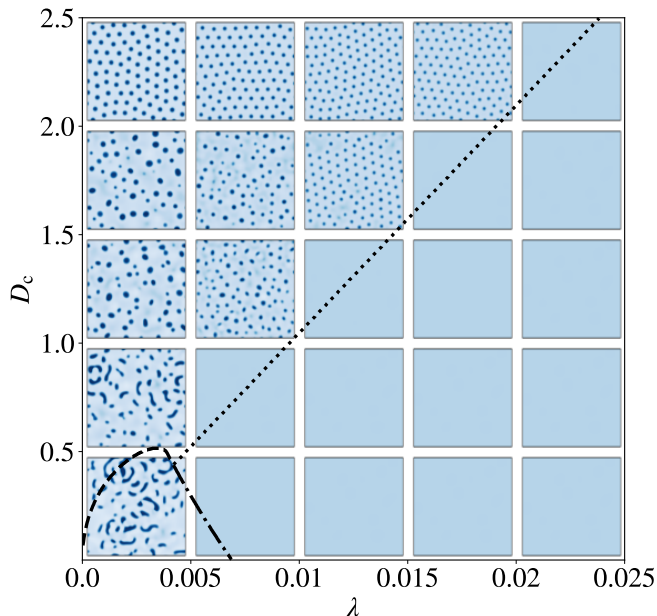


FIG. 3. Phase diagram of the hydrodynamic model in the AMR at $n_0 = 20$ and $\zeta = 22$. The LSA predictions for the phase boundaries are indicated by the dotted (H-S boundary), the dash-dotted (H-O boundary), and the dashed (S-O boundary) lines. For comparison, snapshots of particle distribution (with darker regions indicating higher density) obtained by hydrodynamic simulations are shown together. The values of λ and D_c for each snapshot correspond to the coordinates of its center.

nism of MIPS for $\lambda > 0$ is fundamentally different from the corresponding mechanism for $\lambda = 0$, which explains the discontinuous change of the phase boundary.

To check the validity of the LSA, we perform numerical simulations of Eq. (5) via the pseudo-spectral method. In Fig. 1(b), we show the phase boundary (indicated by a dotted curve) predicted by the LSA together with snapshots of the numerical simulations at $t = 2 \times 10^3$ as the global mean concentration n_0 and the deceleration parameter ζ are varied within the physical regime (the grayed-out area corresponds to the unphysical regime where $v(\rho, n) < 0$). Note that the coordinates of the center of each snapshot indicate the associated values of n_0 and ζ . Clearly, the predicted boundary correctly separates the homogeneous snapshot from the phase-separated ones.

We also show how the phase-separated patterns evolve with time in Fig. 2. For the vanilla MIPS, whether phase separation occurs via bubble or cluster formation depends on the global density ρ_0 of particles. However, by introducing chemokinetic effects, the particles can be made to form clusters [as shown in Fig. 2(a)] or bubbles [as shown in Fig. 2(b)] even at the same value of ρ_0 by adjusting the global chemical concentration n_0 . This is thanks to the strong anticorrelation between $\rho(\mathbf{r}, t)$ and $n(\mathbf{r}, t)$, which makes the chemicals form clusters (bub-

bles) where the particles form bubbles (clusters). Since large (small) n_0 favors bubble (cluster) formation of the chemicals, the particles are driven to form clusters (bubbles). We also note that the length scale of the bubbles and clusters gradually increases in time, which suggests the coarsening dynamics driven by the Ostwald process.

B. AMR induces small, oscillating clusters

The LSA for the AMR can be done similarly, but it differs from that for the BMR in that \mathcal{B} and \mathcal{C} in Eq. (8) may have different signs ($\mathcal{B} < 0$ and $\mathcal{C} > 0$). The eigenvalues ω_{\pm} , obtained in Eq. (9), may then have nonzero imaginary parts. Thus, the AMR exhibits the O phase in addition to the H and the S phases, which leads to some extra complications in predicting the phase boundaries. Nonetheless, the LSA can be carried out exactly, as detailed in Appendix A. Through the analysis, we can prove that the presence of the particle-chemical coupling ($\lambda > 0$) always broadens the H phase. This confirms our previous expectation (discussed in Sec. II) that the AMR suppresses the MIPS.

Examples of the ζ - n_0 and the D_c - λ phase diagrams for the AMR are shown in Fig. 1(c) and 3, respectively. The LSA prediction for the H-S phase boundary is marked by the dotted line, the H-O boundary by the dash-dotted line, and the S-O boundary by the dashed line. For comparison, we also show the snapshots of the particle density, which are obtained by numerical simulations of Eqs. (5) via the pseudo-spectral method. shown together for comparison, where the coordinates of the center of each square corresponds to the parameters used in the simulation. The predicted H-S and the H-O boundaries, for which we expect the LSA to be exact, are in good agreement with the numerics. In contrast, the O phase seems to be broader than indicated by the predicted S-O boundary, as exemplified by the lower left corner of Fig. 3. Since the LSA is valid only up to linear order in density and concentration fluctuations, it is only natural that the true S-O boundary would deviate from the LSA prediction.

Besides the existence of new phase boundaries, the patterns shown by the AMR vastly differ from those of the BMR. In Fig. 4, we provide close-ups of the representative patterns generated by the AMR in the S and the O phases. Higher-density regions are indicated by darker blue shades, while green is used to show the mean vorticity $\omega = \nabla \times \mathbf{u}$ of the particle flux, where $\mathbf{u} = \mathbf{J}/\rho$ is the local particle velocity defined in terms of the particle current density

$$\mathbf{J} = - \left\{ D \nabla \rho + \frac{v(\rho, n)}{2D_r} \nabla [v(\rho, n) \rho] - \kappa \nabla (\nabla^2 \rho) \right\} \quad (13)$$

appearing in Eq. (5). We note that high vorticity tends to coincide with regions where patterns evolve more rapidly. With these in mind, we can identify at last three notable

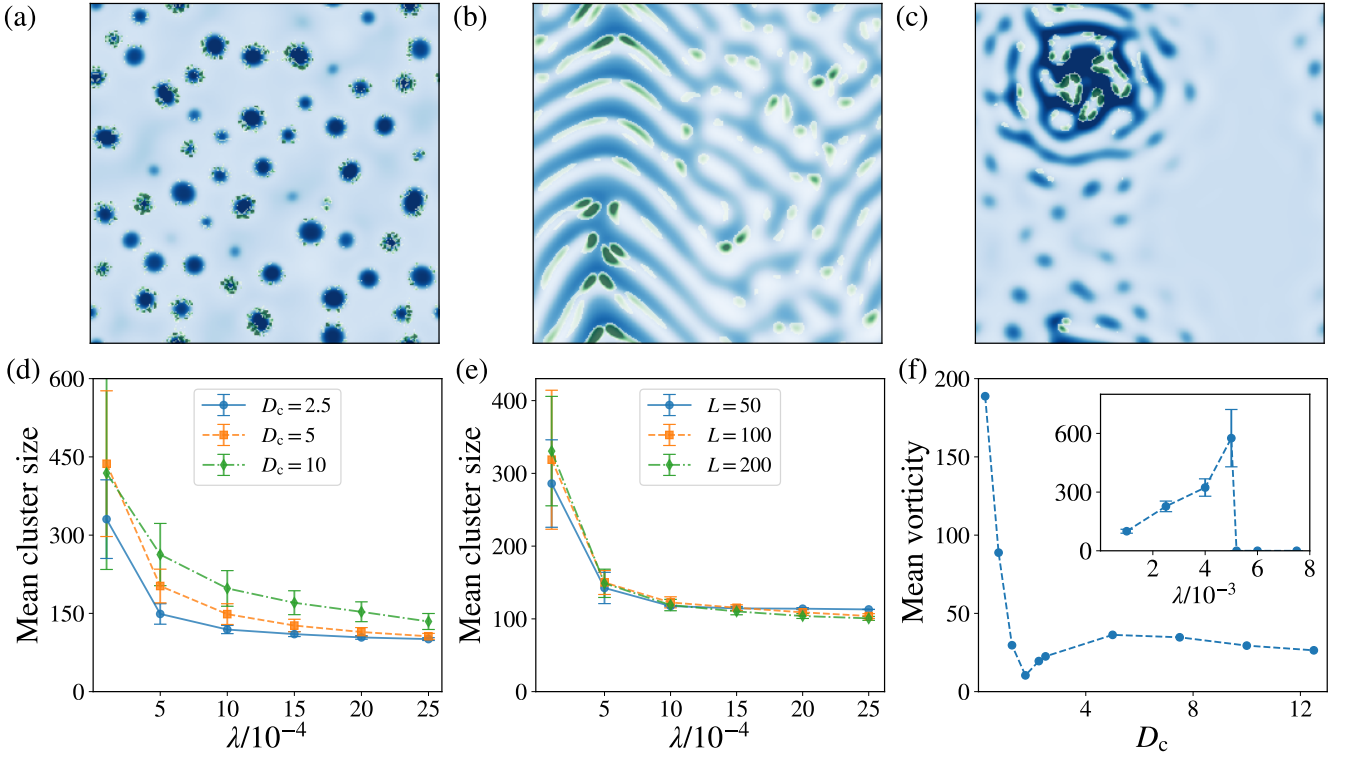


FIG. 4. Phase-separated patterns of the hydrodynamic model in the AMR. Particle density $\rho(\mathbf{r}, t)$ (blue) and the magnitude of local vorticity $|\boldsymbol{\omega}(\mathbf{r}, t)|$ (green) are shown for (a) diffusive droplets ($\lambda = 0.0025$, $D_c = 1.75$, $n_0 = 10$, $\zeta = 22$), (b) ballistic bands ($\lambda = 0.01$, $D_c = 1$, $n_0 = 17.5$, $\zeta = 28.5$), and (c) radiating ripples ($\lambda = 0.01$, $D_c = 1$, $n_0 = 23.5$, $\zeta = 28.5$). (d, e) Mean cluster size in the S phase as λ is varied. The error bars indicate the standard deviation of cluster size. (f) Mean vorticity as D_c is varied for $\lambda = 0.0025$ and (inset) as λ is varied for $D_c = 0.25$. Note that $n_0 = 20$ and $\zeta = 22$ in (d–f).

patterns, namely diffusive droplets [see Fig. 4(a)] well within the S phase, ballistic bands near the boundaries of the O phase [see Fig. 4(b)], and radiating ripples well within the O phase [see Fig. 4(c)]. It seems that the latter two patterns are essentially the same, the only difference being that radiating ripples have a smaller length scale. This is also corroborated by the LSA, which shows that the unstable oscillating fluctuations tend to exhibit shorter wavelengths in the regimes of radiating ripples compared to ballistic bands.

Since all these patterns exist beyond the regime where the LSA is valid, in the following we rely on the results of hydrodynamic simulations to examine how they depend on various control parameters.

Let us first look into the properties of the diffusive droplets. As indicated by Fig. 4(d), the average number of particles forming each droplet (which we call the *mean cluster size*) decreases with λ and increases with D_c . The former is in agreement with our intuition that the particle-chemical coupling in the AMR suppresses the MIPS. The latter is due to the high D_c strongly suppressing the short-wavelength undulations of the chemical concentration. Since all patterns are formed by the particle density and the chemical concentration sharing the same characteristic length scale, this effect also drives the particles to form larger droplets. However, as implied by

the snapshots in Fig. 3, the mean cluster size starts to increase again when D_c decreases below 2.5. This is due to the droplets becoming increasingly motile and actively colliding with each other as the system approaches the S–O boundary.

All these behaviors are in stark contrast to the case of the BMR, where the MIPS eventually forms a single macroscopic particle cluster via coarsening, as exemplified by Fig. 2. Indeed, Fig. 4(e) indicates that the mean cluster size does not change appreciably with the system size L when $\lambda > 0$. In other words, the size of each droplet stays finite, and the S phase of the AMR exhibits microphase separation.

Now, we examine how the system changes quantitatively as it transitions from the S phase with diffusive droplet to the O phase with ballistic bands and radiating ripples. As already shown in Figs. 4(a)–(c), the latter two patterns exhibit spatially extended regions of high vorticity, reflecting their large-scale evolution in time. In contrast, the high-vorticity regions for the diffusive droplets are limited to the droplet boundaries. This implies that the mean vorticity

$$\text{Mean vorticity} \equiv \frac{1}{L^2} \int d^2\mathbf{r} |\nabla \times \mathbf{u}(\mathbf{r})|^2 \quad (14)$$

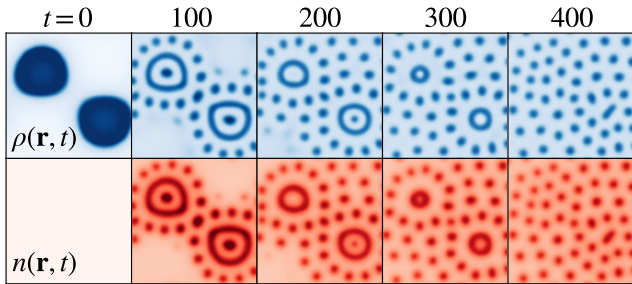


FIG. 5. Evolution of particle density $\rho(\mathbf{r},t)$ and chemical concentration $n(\mathbf{r},t)$ in the hydrodynamic simulation starting from the initial state with two particle clusters and the uniform concentration. The parameters are given by $n_0 = 20$, $\zeta = 25$, $D_c = 0.1$, and $\lambda = 0.5$, which corresponds to the S phase.

can be used as an indicator of the O phase. Indeed, Fig. 4(f) shows that the mean vorticity dramatically increases as D_c is decreased for $\lambda = 0.0025$, crossing the S–O boundary shown in Fig. 3. Notably, even before reaching the S–O boundary, the mean vorticity gradually increases as D_c is decreased, which is then followed by a sharp dip around $D_c = 2$. This nonmonotonic behavior might be due to the individual droplets becoming increasingly motile as D_c is reduced, which then merge together by collisions and shorten the boundaries, thus reducing the high-vorticity regions as well. The inset of Fig. 4(f), which shows the mean vorticity for $D_c = 0.25$ as λ is varied, similarly captures the O phase lying between the S and the H phases in the lower part of Fig. 3.

With the qualitative differences between different patterns thus established, we move onto understanding their underlying dynamics. We first examine how the microphase separation occurs in the S phase, starting from a configuration of two large particle clusters and the uniform chemical distribution. As depicted in Fig. 5, these large particle clusters quickly disintegrate into smaller clusters (including some ring-like structures), while the chemical develops a pattern that overlaps almost exactly with the particle distribution. Then these intermediate particle-chemical clusters gradually shrink, letting the other particle-chemical clusters grow at their expense until all clusters have roughly the same size. This suggests the reverse Ostwald process underlying the microphase separation, which was also found to play a crucial role in the microphase separation of generic single-species scalar active matter [15].

We also look into how the particle-chemical coupling creates the traveling patterns in the O phase. When D_c is large, the chemical concentration is slaved to the particle density, so that their undulations overlap almost exactly as shown in Fig. 6(a) and (b). This leads to the diffusive droplets observed in the S phase. In contrast, when D_c is sufficiently small, the particle and the chemical dynamics may have comparable time scales, in which case the following scenario becomes possible. Suppose

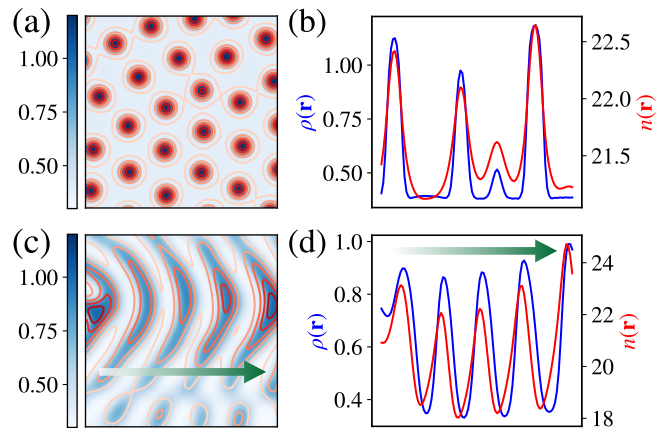


FIG. 6. Profiles of particle density $\rho(\mathbf{r})$ and chemical concentration $n(\mathbf{r})$ in (a, b) the S phase ($D_c = 2.25$, $\lambda = 0.0025$, $\rho_0 = 20$, $\zeta = 22$) and (c, d) the O phase ($D_c = 1$, $\lambda = 0.01$, $\rho_0 = 25.5$, $\zeta = 17.5$). Note that (b) and (d) are cross sections of (a) and (c), respectively. The arrows in (c) and (d) indicate the directions in which the patterns move.

that the particle density undulations are slightly shifted to the right with respect to those of the chemical concentration. Then, for each density peak, the chemical concentration is lower (higher) on the right (left), decreasing (increasing) the speed of particles there. This means that particles tend to accumulate on the right and evaporate on the left, making the peak travel to the right. The concentration peak follows the density peak but cannot catch up for a prolonged period of time since D_c is small. This is precisely what happens for the density and the concentration fields shown in Figs. 6(c) and (d), which exhibit band-like patterns traveling to the right.

It is important to note that these traveling patterns in the O phase are consequences of the nonreciprocity reflected in the different signs of \mathcal{B} and \mathcal{C} appearing in Eq. (8). Known examples of traveling bands share the same property, such as the Vicsek model [31] in which the interparticle interactions are nonreciprocal, and the multispecies scalar active matter obeying the non-reciprocal Cahn–Hilliard dynamics [32, 33]. In a sense, our model can also be regarded as a multispecies scalar active matter with continuously varying self-propulsion speed. However, unlike the previous examples, the band patterns of our model are not necessarily straight or aligned in a single direction, as clearly exemplified in Figs. 4(b) and (c).

IV. PARTICLE-BASED SIMULATIONS

Thus far, we have discussed the phase separation and pattern formation behaviors of the hydrodynamic model. It still remains to be checked whether the same behaviors persist for the original particle-based models from which the hydrodynamic model is derived. In this sec-

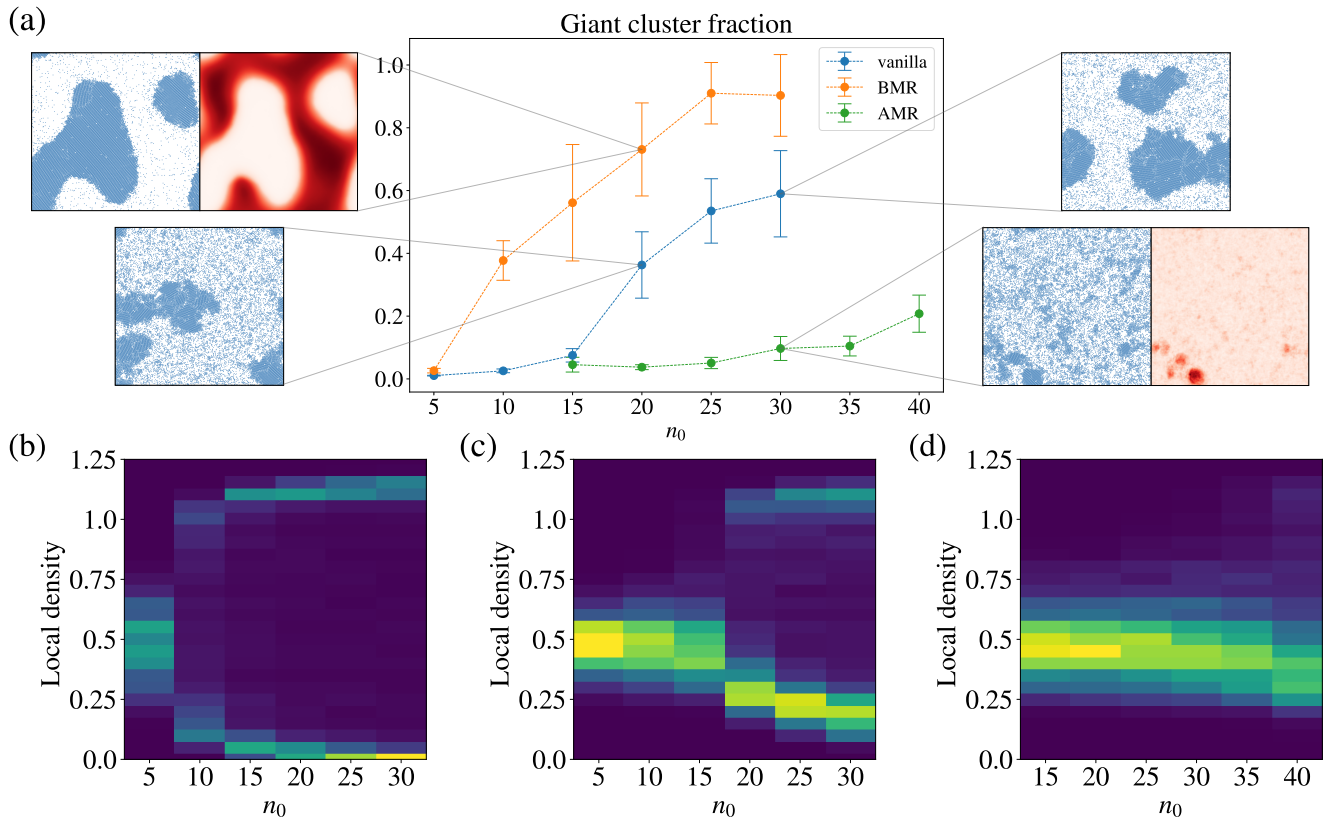


FIG. 7. (a) Fraction of particles belonging to the largest cluster (identified using the DBSCAN algorithm) as the global chemical concentration n_0 is varied in the particle-based model with the WCA potential. Error bars are obtained using six different realizations. Snapshots of the particle (blue) and chemical (red) distributions are shown together. We use $\sigma = 1/2$, $u_0 = 100$, $\lambda = 0.1$, $D_c = 1$, and $L = 200$, with the other parameters identical to those used in Fig. 1. (b–d) Histograms of local particle density as n_0 is varied for (b) the BMR, (c) the vanilla model, and (d) the AMR. All physical quantities and snapshots are measured at time $t = 200$.

tion, we address the issue using the ABPs interacting mechanically via the Weeks–Chandler–Andersen (WCA) potential and the quorum-sensing ABPs whose parameters closely match those of the hydrodynamic model.

A. Mechanically interacting ABPs

Here, we directly simulate the particle-based model following Eqs. (1)–(4), with the short-range repulsion between particles given by the WCA potential

$$V(r) = \begin{cases} 4u_0 \left[\left(\frac{\sigma}{r} \right)^{12} - \left(\frac{\sigma}{r} \right)^6 \right] + u_0 & \text{for } r < 2^{1/6}\sigma \\ 0 & \text{for } r \geq 2^{1/6}\sigma \end{cases}, \quad (15)$$

where σ is the effective radius of each particle. We note that the Dirac delta function appearing in Eqs. (3) and (4) are discretized in the simulation, so that its value becomes 1 only when the particle is in the grid corresponding to \mathbf{r} and 0 otherwise.

To verify whether the BMR (AMR) facilitates (sup-

presses) the MIPS as shown for the hydrodynamic model, we let the above model evolve from a homogeneous initial state to $t = 200$ and observe its phase separation behaviors. In Fig. 7(a), we show the fraction of particles belonging to the largest cluster (also called the *giant cluster*) for the BMR, the AMR, and the vanilla model using the same set of parameters (except for $\lambda = 0$ used in the vanilla model). The BMR develops a larger particle cluster compared to the vanilla model, with the chemical concentration becoming higher outside the particle cluster. In contrast, the AMR strongly suppresses the growth of clusters, with the chemical concentration becoming higher inside the particle cluster. It is also notable that the giant clusters formed by the BMR have smooth interfaces, while those formed by the AMR tends to be of rugged shapes. This rules out the presence of the Ostwald process driven by the positive interfacial tension in the AMR, which is crucial for the large-scale phase separation in the BMR.

Using the histograms of the local particle density, we also check whether phase separation occurs for the BMR [see Fig. 7(b)], the vanilla model [see Fig. 7(c)], and the AMR [see Fig. 7(d)] at different values of n_0 . For the

BMR, the separation between dense and sparse regions occurs at the smallest value of n_0 among the three cases, and the density gap at a fixed value of n_0 is also the largest. For the AMR, on the contrary, the phase separation can hardly be detected by the histograms. In other words, the AMR does not exhibit phase separation, or the dense particle clusters are too small to be captured by the histograms.

These results indicate that the BMR facilitates the large-scale MIPS, whereas the AMR suppresses the MIPS and allows only microphase separation. These results are consistent with the behaviors of the hydrodynamic model. However, the O phase of the AMR is not clearly observable in this particle-based model. This may be because the microscopic noises, which are neglected in the hydrodynamic model, overwhelm the oscillating patterns. This raises the question of whether the O phase of the AMR identified by the LSA is merely an artifact of the hydrodynamic model. We address this issue using a different particle-based model below.

B. Quorum-sensing ABPs

As a particle-based model more easily comparable with the hydrodynamic counterpart, here we introduce the *quorum-sensing ABPs*. While their dynamics share Eqs. (2)–(4) with the mechanically interacting ABPs, Eq. (1) is replaced with

$$\dot{\mathbf{r}}_k(t) = \mu v(\varrho_{\text{loc}}(\mathbf{r}_k, t), n(\mathbf{r}_k, t)) \mathbf{e}_k + \sqrt{2\mu T} \boldsymbol{\xi}_k, \quad (16)$$

where the magnitude of self-propulsion is given by

$$v(\varrho_{\text{loc}}, n) = \alpha n - \varrho_{\text{loc}} \zeta \quad (17)$$

for the local particle density evaluated as

$$\varrho_{\text{loc}}(\mathbf{r}, t) = \int d^2\mathbf{r}' K(\mathbf{r} - \mathbf{r}') \sum_{k'=1}^N \frac{1}{N} \delta(\mathbf{r}' - \mathbf{r}_{k'}(t)). \quad (18)$$

The kernel $K(\mathbf{r})$ should be positive only within a finite range, which is chosen to be

$$K(\mathbf{r}) = \begin{cases} 1/\pi & \text{if } |\mathbf{r}| < 1, \\ 0 & \text{otherwise.} \end{cases} \quad (19)$$

This ensures that each particle decelerates according to the mean-field density in its neighborhood rather than via repulsive pairwise interactions. The model thereby suppresses the effects of microscopic fluctuations, which wash out the phase-separated patterns predicted by the hydrodynamic theory. Such mean-field interactions between particles is possible when they are capable of quorum sensing, hence the name *quorum-sensing ABPs*.

The quorum-sensing ABPs have some advantages compared to the mechanically interacting ABPs. First, the parameters of the model are identical to those of the hy-

drodynamic model, making quantitative comparison between the models easier. The only hydrodynamic parameter not explicitly built into the model is κ , but applying the coarse-graining scheme of [11], linearizing the equations with respect to the homogeneous profile, and neglecting higher-order derivatives, we can identify

$$\kappa = \frac{\rho_0 \zeta (\alpha n_0 - \rho_0 \zeta)}{8D_r} - \frac{D}{D_r} D_{\text{eff}}. \quad (20)$$

By evaluating this quantity, we can determine which hydrodynamic model corresponds to a given system of quorum-sensing ABPs. The second advantage is that, since there is no short-range repulsion, the simulation of quorum-sensing ABPs can work even with relatively large time steps without blowing up. Indeed, we use $\Delta t = 10^{-3}$ for the quorum-sensing ABPs, while $\Delta t = 10^{-5}$ has to be used for the mechanically interacting ABPs.

Let us now examine how the behaviors of the quorum-sensing ABPs compare with the hydrodynamic model. For the BMR, as detailed in Appendix A, the boundary between the H and S phases is determined only by infinite-wavelength features of the system. The property, which is also reflected in the absence of κ in Eq. (10) for the phase boundary of the BMR, implies that the phase boundary of the quorum-sensing ABPs coincides exactly with that of the hydrodynamic theory. This is verified by Fig. 8(a), which shows the snapshots of the simulations of the quorum-sensing ABPs at $t = 4 \times 10^2$ (starting from uniform configurations at $t = 0$) together with the phase boundary predicted by Eq. (10) (marked by the dotted line). As was the case for the hydrodynamic model (see Fig. 2), the system tends to form more concentrated particle clusters for higher n_0 , while sparse regions broaden at the expense of dense regions as n_0 is decreased. If the system is allowed to evolve even longer (to $t = 4 \times 10^2$), different clusters merge via the Ostwald process, forming large-scale patterns (see Fig. S2) also observed in the hydrodynamic model.

For the AMR, the short-wavelength features do affect the phase boundaries, so the correspondence between the quorum-sensing ABPs and the hydrodynamic model cannot be exact. Still, Fig. 8(b) and Supplementary Movies XXX suggest some qualitative agreements between the two. At fixed D_c , the snapshots show that the particle clusters shrink with increasing λ . This is also confirmed by the λ -dependence of the mean cluster size at $D_c = 2.5$ shown in the inset of Fig. 9, which also reveals that the mean cluster size does not change appreciably with the system size L . These results are consistent with the existence of a transition from the S phase with microphase separation to the H phase predicted by the hydrodynamic theory.

Meanwhile, when λ is fixed at a small value, the snapshots in Fig. 8(b) indicate that the particle clusters fluctuate more vigorously as D_c is reduced. As done in the case of the hydrodynamic model, we may use the mean vorticity to quantify this trend; however, since the cal-

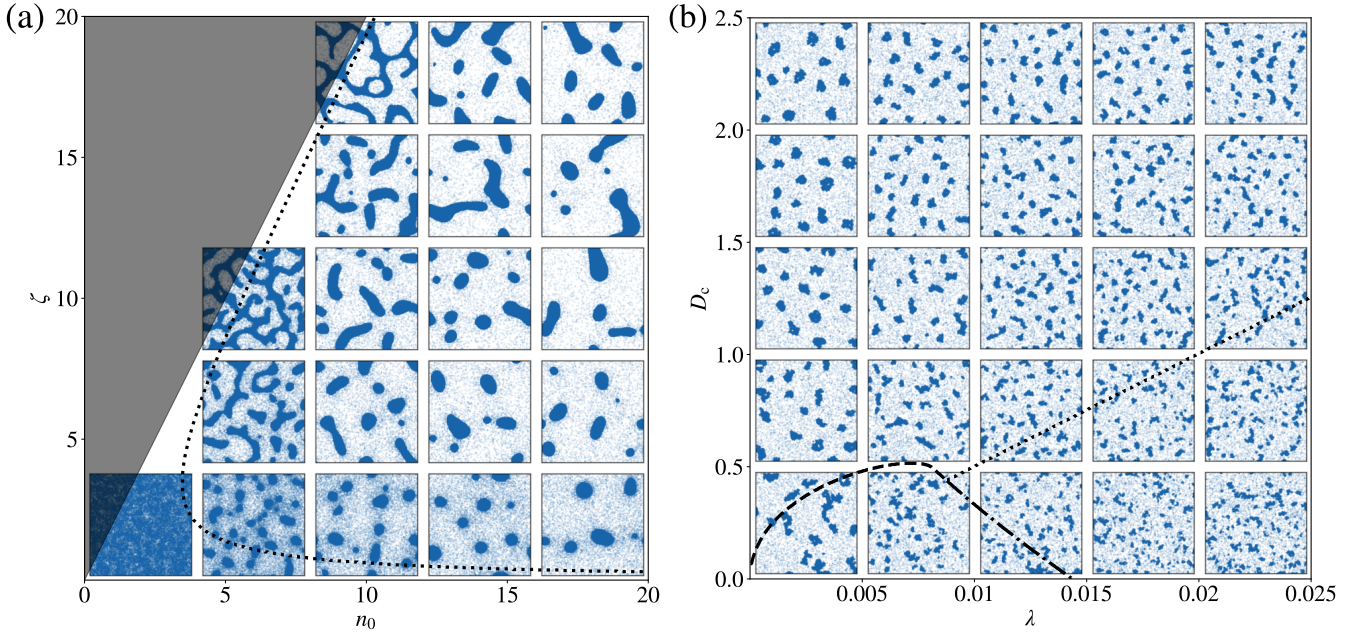


FIG. 8. Phase diagram of the quorum-sensing ABP model in (a) the BMR with $\lambda = 0.5$, $D_c = 10$, $L = 400$, $t = 4 \times 10^2$ and (b) the AMR with $n_0 = 20$, $\zeta = 22$, $L = 400$, $t = 1.6 \times 10^3$. The LSA predictions for the phase boundaries (at $\kappa = 4.791667$) are indicated by the dotted (H-S boundary), the dash-dotted (H-O boundary), and the dashed (S-O boundary) lines. For comparison, snapshots of particle distribution (with darker regions indicating higher density) obtained by particle-based simulations are shown together. The central coordinates of each snapshot correspond to the parameters used in the simulation. Note that the snapshots in (b) have been cropped to the size of 200 times 200 for better visibility.

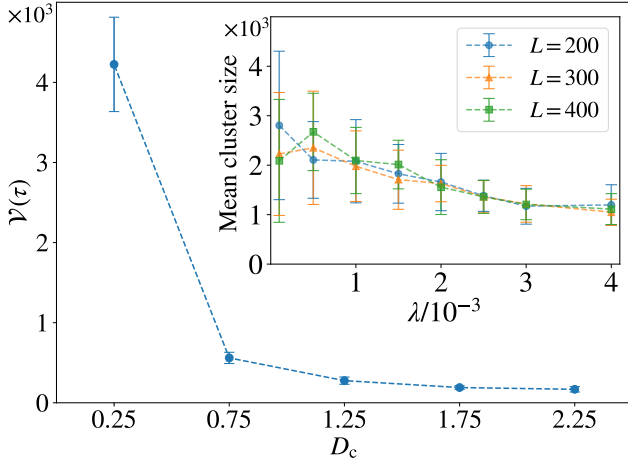


FIG. 9. Dependence of the time-variability $\mathcal{V}(\tau)$ on D_c in the AMR model of QS simulation, evaluated with $\tau = 200$, $L_{\text{win}} = 35$. Other parameters: $\lambda = 0.0025$, $n_0 = 20$, $\zeta = 22$. Inset: mean (round marker) and standard deviation (error bar) of cluster sizes for $n_0 = 20$, $\zeta = 22$, $D_c = 2.5$ at $t = 2 \times 10^3$.

culcation of vorticity requires coarse-graining the particle configuration that introduces extra numerical error, we resort to an alternative measure. For some $\tau > 0$, we

define the time-variability

$$\mathcal{V}_\tau \equiv \int dt \int d^2\mathbf{r} |\bar{n}(\mathbf{r}, t + \tau) - \bar{n}(\mathbf{r}, t)|^2, \quad (21)$$

where $\bar{n}(\mathbf{r}, t)$ is the average of the chemical concentration $n(\mathbf{r}, t)$ over a square of side length L_{win} centered at the position \mathbf{r} . By examining how large \mathcal{V}_τ can be for a suitable choice of τ and L_{win} , one can quantify the magnitude, time scale, and length scale of oscillations present in the system. At $\lambda = 0.0025$, choosing $\tau = 200$ and $L_{\text{win}} = 35$, we observe a dramatic increase of \mathcal{V}_τ as D_c is lowered [see Fig. 9]. Moreover, the behaviors of \mathcal{V}_τ also suggest that the length scale of cluster patterns tends to decrease with increasing λ , as shown in Fig. S3. These support the existence of the S-O and the H-O boundaries predicted by the hydrodynamic theory.

We note that the ballistic bands and the radiating ripples generated by the hydrodynamic model are not clearly observable for the quorum-sensing ABPs. This may be due to the microscopic fluctuations, which are not fully removed by introducing mean-field interactions, destroying such large-scale patterns. Still, our results thus far imply that a particle-based model can exhibit all of the three phases predicted by the hydrodynamic theory.

V. SUMMARY AND OUTLOOK

We showed that chemokinesis combined with chemical consumption can profoundly affect the collective behaviors of active particles. For the BMR, the chemical consumption is increased inside dense particle clusters, resulting in lower chemical concentration there and more robust clusters compared to the vanilla case. Conversely, when particles in the AMR are clustered, the enhanced chemical consumption within the region reduces cluster size or even leads to the evaporation of temporary clusters. We validated our scenarios through three approaches: linear stability analysis, numerical simulations of the coarse-grained hydrodynamic equations, and particle simulations.

To our best knowledge, this study is the first to demonstrate the importance of chemical consumption mechanism on the patterns of active matter. Future researches may contain similar analyses for models beyond scalar active matter, including models with polar order, topological defects, etc. Moreover, various mechanical abilities of active matter, such as enhanced transport and current rectification may also be modified by chemical consumption. This may affect the performance of collective machines utilizing active matter, and therefore should be investigated further.

Acknowledgments. — This work was supported by the National Research Foundation of Korea (NRF) grant funded by the Korea government (MSIT) (No. RS-2023-00218318).

Appendix A: Linear stability analysis

Here we provide details of the LSA whose results are used in Sec. III. Suppose that the density ρ and the concentration n are weakly perturbed around their homogeneous values ρ_0 and n_0 , respectively:

$$\rho = \rho_0 + \delta\rho, \quad n = n_0 + \delta n. \quad (\text{S1})$$

Using these in Eq. (5), the time evolution of $\delta\rho$ is expanded to linear order as

$$\delta\dot{\rho} = D_{\text{eff}}\nabla^2\delta\rho - \kappa\nabla^2(\nabla^2\delta\rho) + \frac{\alpha\rho_0(\alpha n_0 - \rho_0\zeta)}{2D_r}\nabla^2\delta n, \quad (\text{S2})$$

where

$$D_{\text{eff}} \equiv D + \frac{(\alpha n_0 - \rho_0\zeta)(\alpha n_0 - 2\rho_0\zeta)}{2D_r} \quad (\text{S3})$$

is the effective diffusion coefficient governing the collective relaxation of the density profile. Meanwhile, δn evolves in the linear regime according to

$$\delta\dot{n} = D_c\nabla^2\delta n - \lambda n_0\delta\rho - \lambda\rho_0\delta n \quad (\text{S4})$$

for the BMR and

$$\begin{aligned} \delta\dot{n} = & D_c\nabla^2\delta n - \lambda n_0(\alpha n_0 - 2\rho_0\zeta)\delta\rho \\ & - \lambda\rho_0(2\alpha n_0 - \rho_0\zeta)\delta n \end{aligned} \quad (\text{S5})$$

for the AMR.

Now, taking the Fourier components $\delta\rho = \delta\rho_0 e^{i\mathbf{q}\cdot\mathbf{r}+\omega t}$ and $\delta n = \delta n_0 e^{i\mathbf{q}\cdot\mathbf{r}+\omega t}$, Eqs. (S2), (S4), and (S5) can be rewritten as an eigenvalue equation

$$\begin{pmatrix} \mathcal{A} & \mathcal{B} \\ \mathcal{C} & \mathcal{D} \end{pmatrix} \begin{pmatrix} \delta\rho_0 \\ \delta n_0 \end{pmatrix} = \omega \begin{pmatrix} \delta\rho_0 \\ \delta n_0 \end{pmatrix}, \quad (\text{S6})$$

where

$$\begin{aligned} \mathcal{A} &= -\kappa q^4 - D_{\text{eff}} q^2, \\ \mathcal{B} &= -\left[\frac{\alpha\rho_0(\alpha n_0 - \rho_0\zeta)}{2D_r}\right] q^2, \\ \mathcal{C} &= \begin{cases} -\lambda n_0 & (\text{BMR}) \\ -\lambda n_0(\alpha n_0 - 2\rho_0\zeta) & (\text{AMR}) \end{cases}, \\ \mathcal{D} &= \begin{cases} -D_c q^2 - \lambda\rho_0 & (\text{BMR}) \\ -D_c q^2 - \lambda\rho_0(2\alpha n_0 - \rho_0\zeta) & (\text{AMR}) \end{cases}. \end{aligned} \quad (\text{S7})$$

Solving the characteristic equation

$$\omega^2 - (\mathcal{A} + \mathcal{D})\omega + \mathcal{A}\mathcal{D} - \mathcal{B}\mathcal{C} = 0, \quad (\text{S8})$$

the eigenvalues are obtained as

$$\omega_{\pm} = \frac{1}{2} \left[(\mathcal{A} + \mathcal{D}) \pm \sqrt{(\mathcal{A} - \mathcal{D})^2 + 4\mathcal{B}\mathcal{C}} \right]. \quad (\text{S9})$$

Among the two eigenvalues, the one with the larger real part always dominates the long-time behavior. If $(\mathcal{A} - \mathcal{D})^2 + 4\mathcal{B}\mathcal{C} > 0$, then ω_+ is the dominant one. If $(\mathcal{A} - \mathcal{D})^2 + 4\mathcal{B}\mathcal{C} \leq 0$, then both ω_+ and ω_- are equally dominant.

1. Case of the BMR

In this case, $\mathcal{B}\mathcal{C}$ is always positive. Then Eq. (S9) ensures that both eigenvalues are real, with the boundary between the H and the S phases determined by when ω_+ changes its sign. In the S phase, near the phase boundary, we must have $\omega_+ > 0$ and $\omega_- < 0$. By examining the quadratic left-hand side of Eq. (S8), one can see that this is equivalent to the condition $\mathcal{A}\mathcal{D} - \mathcal{B}\mathcal{C} < 0$. By simple algebra, we obtain $\mathcal{A}\mathcal{D} - \mathcal{B}\mathcal{C} = q^2 h(q^2)$, where

$$\begin{aligned} h(q^2) = & \kappa D_c q^4 + (D_{\text{eff}} D_c + \kappa \lambda \rho_0) q^2 + \lambda \rho_0 D_{\text{eff}} \\ & - \frac{\lambda \rho_0}{2D_r} \alpha n_0 (\alpha n_0 - \rho_0 \zeta) \end{aligned} \quad (\text{S10})$$

is a quadratic function of q^2 . For $h(q^2) < 0$ to be satisfied for some range of q^2 , there are two possible cases. First, if $h(0) < 0$, there exists an interval $q^2 \in [0, q_*^2]$ in which

$h(q^2) < 0$ holds. This condition is equivalent to

$$D_{\text{eff}} < \frac{\alpha n_0}{2D_r}(\alpha n_0 - \rho_0 \zeta). \quad (\text{S11})$$

Second, if $h(0) > 0$, then $h'(0) < 0$ must hold for $h(q^2)$ to be negative for some interval $q^2 \in [q_-^2, q_+^2]$. In this case,

$$D_{\text{eff}} > \frac{\alpha n_0}{2D_r}(\alpha n_0 - \rho_0 \zeta) \quad (\text{S12})$$

and

$$D_{\text{eff}} < -\frac{\kappa \lambda \rho_0}{D_c} \quad (\text{S13})$$

must be satisfied simultaneously, which is impossible. Thus, only Eq. (S11) determines the S phase, which can also be written as

$$D < \frac{\rho_0 \zeta (\alpha n_0 - \rho_0 \zeta)}{D_r}. \quad (\text{S14})$$

The phase boundary obtained in Eq. (10) follows directly from this result. Notably, the discussion thus far shows that the boundary of the H phase in the BMR is determined only by infinite-wavelength fluctuations ($q = 0$), reflecting that the BMR is capable of large-scale phase separation even in the linear regime.

Meanwhile, in the absence of particle-chemical coupling ($\lambda = 0$), $h(q^2) < 0$ holds for some range of q^2 if and only if $h'(0) = D_{\text{eff}} D_c < 0$. This implies that the vanilla model exhibits MIPS for $D_{\text{eff}} < 0$ (which is clearly more stringent than Eq. (S11) for the BMR), from which Eq. (12) is derived.

2. Case of the AMR

In this case, \mathcal{BC} may be negative, allowing for nonvanishing imaginary parts of the eigenvalues ω_{\pm} . Indeed, it turns out that the AMR exhibits all the three different phases (H, S, and O). In the following, we elaborate on how to determine the boundaries of those phases.

Let us first determine the boundaries of the H phase, which requires that the real part of ω_{\pm} is negative for all q^2 . Due to the quadratic nature of Eq. (S8), the condition $\text{Re } \omega_{\pm} < 0$ is fulfilled when both $\mathcal{AD} - \mathcal{BC} > 0$ and $\mathcal{A} + \mathcal{D} < 0$ are true.

We start with the first inequality. By some algebra, we obtain $\mathcal{AD} - \mathcal{BC} = q^2 h(q^2)$, where

$$\begin{aligned} h(q^2) = & \kappa D_c q^4 + [D_{\text{eff}} D_c + \kappa \lambda \rho_0 (2\alpha n_0 - \rho_0 \zeta)] q^2 \\ & + \lambda \rho_0 D_{\text{eff}} (2\alpha n_0 - \rho_0 \zeta) \\ & - \frac{\lambda \rho_0}{2D_r} \alpha n_0 (\alpha n_0 - \rho_0 \zeta) (\alpha n_0 - 2\rho_0 \zeta) \end{aligned} \quad (\text{S15})$$

is a quadratic function of q^2 . If the coefficient of q^2 is positive, the minimum of $h(q^2)$ is located at $q^2 = 0$.

Then, $\mathcal{AD} - \mathcal{BC} > 0$ is equivalent to $h(0) > 0$. These imply

$$D_{\text{eff}} > \max \left[-\frac{\kappa \lambda \rho_0}{D_c} (2\alpha n_0 - \rho_0 \zeta), \frac{\alpha n_0 (\alpha n_0 - \rho_0 \zeta) (\alpha n_0 - 2\rho_0 \zeta)}{2D_r (2\alpha n_0 - \rho_0 \zeta)} \right]. \quad (\text{S16})$$

On the other hand, if the coefficient of q^2 is negative, the minimum of $h(q^2)$ is located at the axis of symmetry $q^2 = -[D_{\text{eff}} D_c + \kappa \lambda \rho_0 (2\alpha n_0 - \rho_0 \zeta)] / (2\kappa D_c)$. Thus, $\mathcal{AD} - \mathcal{BC} > 0$ requires

$$\begin{aligned} & \lambda \rho_0 D_{\text{eff}} (2\alpha n_0 - \rho_0 \zeta) - \frac{\lambda \rho_0}{2D_r} \alpha n_0 (\alpha n_0 - \rho_0 \zeta) (\alpha n_0 - 2\rho_0 \zeta) \\ & - \frac{1}{4\kappa D_c} [D_{\text{eff}} D_c + \kappa \lambda \rho_0 (2\alpha n_0 - \rho_0 \zeta)]^2 > 0, \end{aligned} \quad (\text{S17})$$

which is quadratic in D_{eff} and can be solved analytically.

Next, we check $\mathcal{A} + \mathcal{D} < 0$, which can be written as a quadratic inequality

$$\kappa q^4 + (D_{\text{eff}} + D_c) q^2 + \lambda \rho_0 (2\alpha n_0 - \rho_0 \zeta) > 0. \quad (\text{S18})$$

The inequality is always satisfied when $D_{\text{eff}} + D_c > 0$, as all the other coefficients are positive. When $D_{\text{eff}} + D_c \leq 0$, the minimum value of the quadratic function must be positive, that is,

$$\lambda \rho_0 (2\alpha n_0 - \rho_0 \zeta) - \frac{(D_{\text{eff}} + D_c)^2}{4\kappa} > 0. \quad (\text{S19})$$

Combining all these results, $\mathcal{A} + \mathcal{D} < 0$ is equivalent to

$$D_{\text{eff}} > -D_c - 2\sqrt{\kappa \lambda \rho_0 (2\alpha n_0 - \rho_0 \zeta)}. \quad (\text{S20})$$

Based on the above, one can fully determine the boundaries of the H phase. Here we refrain from giving the explicit expressions for the corresponding values of D_{eff} , which is a rather tedious task. Instead, we note that setting $\lambda > 0$ broadens the ranges of D_{eff} associated with the H phase. This can be seen through the following argument. First, we observe that Eqs. (S16) and (S17) imply

$$D_{\text{eff}} > \frac{\alpha n_0 (\alpha n_0 - \rho_0 \zeta) (\alpha n_0 - 2\rho_0 \zeta)}{2D_r (2\alpha n_0 - \rho_0 \zeta)}. \quad (\text{S21})$$

Using this inequality in Eq. (S15), we obtain

$$h(q^2) \geq \kappa D_c q^4 + D_{\text{eff}} D_c q^2, \quad (\text{S22})$$

with the equality holding if and only if $\lambda = 0$. This means that $\mathcal{AD} - \mathcal{BC} > 0$ becomes weaker for $\lambda > 0$ than for $\lambda = 0$. Similarly, Eq. (S20) shows that $\mathcal{A} + \mathcal{D} < 0$ becomes weaker for $\lambda > 0$ than for $\lambda = 0$. Since both inequalities are weakened by positive λ , we conclude that the AMR suppresses the MIPS and widens the H phase, just as expected in Sec. II.

	$y < 4x(1-2x)$	$y > 4x(1-2x)$
$x > 1/3$	$q_l^2 < \mathbf{q_-^2} < q_r^2 < \mathbf{q_+^2}$	$q_l^2 < \mathbf{q_-^2} < \mathbf{q_+^2} < q_r^2$
$1/5 < x < 1/3$	$q_l^2 < \mathbf{q_-^2} < q_r^2 < \mathbf{q_+^2}$	$q_l^2 < q_r^2 < \mathbf{q_-^2} < \mathbf{q_+^2}$
$x < 1/5$	$q_l^2 < \mathbf{q_-^2} < q_r^2 < \mathbf{q_+^2}$	$\mathbf{q_-^2} < q_l^2 < q_r^2 < \mathbf{q_+^2}$

TABLE I. Ordering of $q_{l,r}^2$ and q_{\pm}^2 . q_{\pm}^2 are bold-faced to emphasize the changes when transitioning from $y < 4x(1-2x)$ to $y > 4x(1-2x)$.

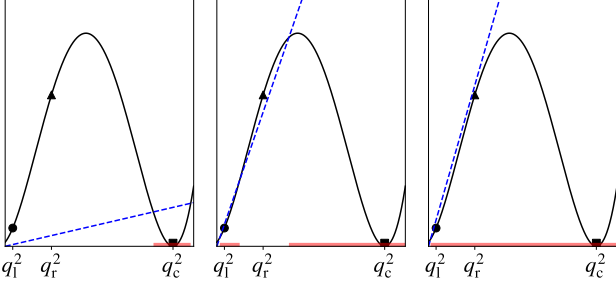


FIG. S1. Illustrations of intervals satisfying $f(q^2) < g(q^2)$. The black solid line represents the quadratic function $f(q^2)$, and the blue dashed line corresponds to the linear function $g(q^2)$. The points of tangency at q_l^2 , q_r^2 , and q_c^2 are marked by the circle, the triangle, and the square, respectively. The intervals of q^2 with $f(q^2) < g(q^2)$ are indicated by thick red horizontal segments.

Now, we turn to the boundaries of the O phase, which corresponds to the case where ω_{\pm} have nonzero imaginary parts (requiring $(\mathcal{A} - \mathcal{D})^2 + 4\mathcal{B}\mathcal{C} < 0$) simultaneously with positive real parts (requiring $\mathcal{A} + \mathcal{D} > 0$).

Let us first check the condition for nonzero imaginary parts. Defining $f(q^2) \equiv (\mathcal{A} - \mathcal{D})^2$ and $g(q^2) \equiv -4\mathcal{B}\mathcal{C}$, the relevant inequality is given by $f(q^2) < g(q^2)$. We note that $f(q^2)$ is the square of a quadratic function with one positive root, which we denote by

$$q_c^2 \equiv -\frac{D_{\text{eff}} - D_c}{2\kappa} \pm \frac{\sqrt{(D_{\text{eff}} - D_c)^2 + 4\kappa\lambda\rho_0(2\alpha n_0 - \rho_0\zeta)}}{2\kappa}. \quad (\text{S23})$$

Hence, $f(q^2)$ has a double root at $q^2 = q_c^2$.

Meanwhile, $g(q^2)$ is a linear function of q^2 crossing the origin. Thus, to examine when $f(q^2) < g(q^2)$ is satisfied, it is helpful to check how many lines crossing the origin can be tangent to $f(q^2)$. The point of tangency can be found by solving

$$\frac{f(q^2)}{q^2} = \frac{d}{d(q^2)} f(q^2), \quad (\text{S24})$$

which is equivalent to

$$3\kappa q^4 + (D_{\text{eff}} - D_c)q^2 + \lambda\rho_0(2\alpha n_0 - \rho_0\zeta) = 0. \quad (\text{S25})$$

This equation has real roots if its discriminant satisfies

$$(D_{\text{eff}} - D_c)^2 - 12\kappa\lambda\rho_0(2\alpha n_0 - \rho_0\zeta) \geq 0. \quad (\text{S26})$$

We first consider the case where the above condition is satisfied. Then, the points of tangency are obtained as

$$q_{l,r}^2 = -\frac{D_{\text{eff}} - D_c}{6\kappa} \pm \frac{\sqrt{(D_{\text{eff}} - D_c)^2 - 12\kappa\lambda\rho_0(2\alpha n_0 - \rho_0\zeta)}}{6\kappa}, \quad (\text{S27})$$

where the plus (minus) sign corresponds to q_r (q_l). We note that both q_l^2 and q_r^2 are positive if they have real values. As illustrated in Fig. S1, depending on the slope of $g(q^2)$ (indicated by the dashed line), the intervals of q^2 satisfying the condition $f(q^2) < g(q^2)$ (indicated by the thick horizontal lines) vary. When the slope of $g(q^2)$ is less than that of the tangent line crossing $(q_r^2, f(q_r^2))$ (indicated by the circle), there exists only a single interval satisfying $f(q^2) < g(q^2)$. If the slope of $g(q^2)$ is greater than that of the tangent line crossing $(q_r^2, f(q_r^2))$, the inequality is satisfied everywhere. In the intermediate regime, there are two separate intervals satisfying the inequality, one around q_l^2 and the other around q_c^2 . As discussed earlier, ω_{\pm} have nonzero imaginary parts in these intervals.

The system exhibits the O phase if and only if these intervals of q^2 overlap with those where ω_{\pm} have positive real parts, which requires $\mathcal{A} + \mathcal{D} > 0$. This inequality is satisfied in the interval (q_-^2, q_+^2) , where

$$q_{\pm}^2 = -\frac{D_{\text{eff}} + D_c}{2\kappa} \pm \frac{\sqrt{(D_{\text{eff}} + D_c)^2 - 4\kappa\lambda\rho_0(2\alpha n_0 - \rho_0\zeta)}}{2\kappa}. \quad (\text{S28})$$

To investigate when the intervals overlap, we examine the condition for $q_{l,r}^2 = q_{\pm}^2$, where either of the two values on the left-hand side can be equal to either of the two on the other side. For convenience, we define $x \equiv -D_c/D_{\text{eff}}$ and $y \equiv 4\kappa\lambda\rho_0(2\alpha n_0 - \rho_0\zeta)/D_{\text{eff}}^2$. After some algebra, one can show that $q_{l,r}^2 = q_{\pm}^2$ is satisfied when

$$y = 4x(1-2x). \quad (\text{S29})$$

This equation is useful for checking when the ordering of $q_{l,r}^2$ and q_{\pm}^2 changes. See Table I for all possible orderings. For most cases, we have $q_l^2 < q_-^2 < q_+^2$. Then the interval (q_-^2, q_+^2) overlaps with nonzero imaginary parts of ω_{\pm} if and only if $\Delta(q^2) \equiv f(q^2) - g(q^2)$ becomes negative at $q^2 = q_-^2$ or q_+^2 . In contrast, for $x < 1/5$ and $y > 4x(1-2x)$, the ordering changes to $q_-^2 < q_l^2 < q_+^2$. It is then possible that (q_-^2, q_+^2) fully contains an interval around q_l^2 with nonzero imaginary parts of ω_{\pm} , *e.g.*, the left one of the two intervals indicated by thick horizontal segments in the middle panel of Fig. S1. For this particular case, the O phase requires that at least one among $\Delta(q_-^2)$,

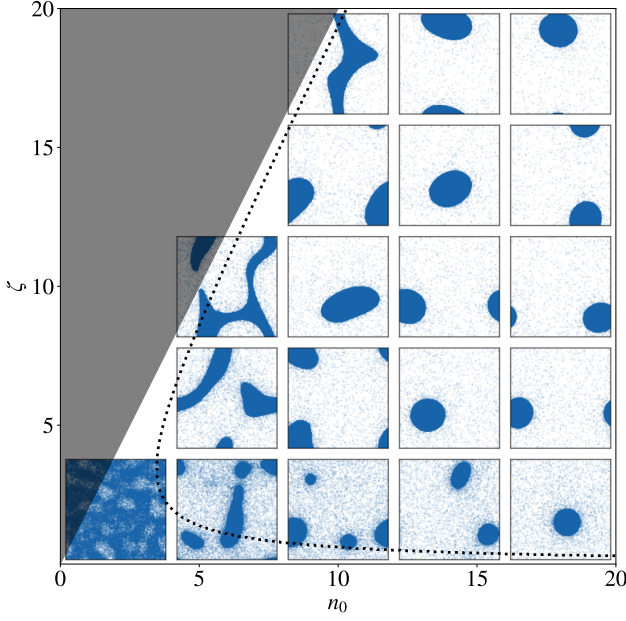


FIG. S2. Phase diagram of the quorum-sensing ABPs in the BMR at $\lambda = 0.5$ and $D_c = 10$. The system size is set to be $L = 400$. The LSA prediction for the H-O boundary is indicated by the dotted curve. The snapshots of particle configurations are taken at $t = 2 \times 10^3$, with the values of ζ and n_0 given by the coordinates of each snapshot's center.

$\Delta(q_1^2)$, and $\Delta(q_+^2)$ must be negative.

Finally, if Eq. (S26) is not satisfied, then $f(q^2) < g(q^2)$ can hold only across a single continuous interval. Then, the O phase only requires that $\Delta(q_+^2)$ or $\Delta(q_-^2)$ be negative. By combining all the conditions discussed so far, the boundaries of the O phase can be fully determined.

In Fig. S2, we show the patterns to which the clusters formed by the quorum-sensing ABPs in Fig. 8(a) evolve if we run the simulations to $t = 2 \times 10^3$. We observe that the small particle clusters merge via the Ostwald process to form large-scale clusters, in agreement with the hydrodynamic prediction. Also note that the particle clusters tend to become elongated as n_0 becomes smaller, which is also observed in the hydrodynamic model.

Appendix B: Extra results for quorum-sensing ABPs

In Fig. S3, we show how the time-variability \mathcal{V}_τ depends on the window size L_{win} for various values of λ along the $D_c = 0.25$ line of Fig. 8(b). We note that the value of L_{win} at which \mathcal{V}_τ is maximized can be regarded as the length scale of oscillating patterns. Then, Fig. S3 indicates that oscillations occur at a shorter length scale with smaller amplitudes as λ grows. This is consistent with the system crossing over from the O phase at small λ to the H phase at large λ .

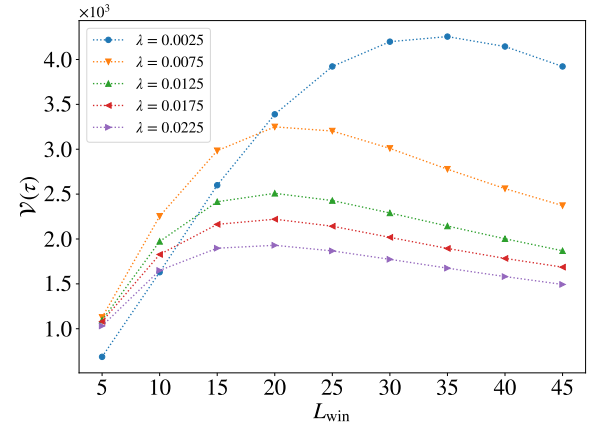


FIG. S3. Time-variability of the quorum-sensing ABPs in the AMR for $\tau = 200$ and $D_c = 0.25$ as λ and L_{win} are varied. The other parameters are identical to those used in Fig. 8(b).

- [1] S. Ramaswamy, *Annu. Rev. Condens. Matter Phys.* **1**, 323 (2010).
- [2] M. C. Marchetti, J. F. Joanny, S. Ramaswamy, T. B. Liverpool, J. Prost, M. Rao, and R. A. Simha, *Rev. Mod. Phys.* **85**, 1143 (2013).
- [3] S. Ramaswamy, *J. Stat. Mech.: Theor. Exp.* **2017**, 054002.
- [4] F. Jülicher, S. W. Grill, and G. Salbreux, *Rep. Prog. Phys.* **81**, 076601 (2018).
- [5] G. Gompper, R. G. Winkler, and T. Speck *et al.*, *J. Phys.: Condens. Matter* **32**, 193001 (2020).
- [6] M. J. Bowick, N. Fakhri, M. C. Marchetti, and S. Ramaswamy, *Phys. Rev. X* **12**, 010501 (2022).
- [7] M. te Vrugt and R. Wittkowski, “A review of active matter reviews,” arXiv:2405.15751 [cond-mat.soft].
- [8] J. Tailleur and M. E. Cates, *Phys. Rev. Lett.* **100**, 218103 (2008).
- [9] Y. Fily and M. C. Marchetti, *Phys. Rev. Lett.* **108**, 235702 (2012).
- [10] G. S. Redner, M. F. Hagan, and A. Baskaran, *Phys. Rev. Lett.* **110**, 055701 (2013).
- [11] J. Bialké, H. Löwen, and T. Speck, *Europhys. Lett.* **103**, 30008 (2013).
- [12] M. E. Cates and J. Tailleur, *Annu. Rev. Condens. Matter Phys.* **6**, 219 (2015).
- [13] R. Wittkowski, A. Tiribocchi, J. Stenhammar, R. J. Allen, D. Marenduzzo, and M. E. Cates, *Nat. Commun.* **5**, 4351 (2014).
- [14] A. Tiribocchi, R. Wittkowski, D. Marenduzzo, and M. E.

- Cates, *Phys. Rev. Lett.* **115**, 188302 (2015).
- [15] E. Tjhung, C. Nardini, and M. E. Cates, *Phys. Rev. X* **8**, 031080 (2018).
- [16] E. Bertin, M. Droz, and G. Grégoire, *Phys. Rev. E* **74**, 022101 (2006).
- [17] J. Stenhammar, A. Tiribocchi, R. J. Allen, D. Maren-

- duzzo, and M. E. Cates, *Phys. Rev. Lett.* **111**, 145702 (2013).
- [18] J. Stenhammar, D. Marenduzzo, R. J. Allen, and M. E. Cates, *Soft Matter* **10**, 1489 (2014).
- [19] C. B. Caporusso, P. Digregorio, D. Levis, L. F. Cugliandolo, and G. Gonnella, *Phys. Rev. Lett.* **125**, 178004 (2020).
- [20] X.-q. Shi, G. Fausti, H. Chaté, C. Nardini, and A. Solon, *Phys. Rev. Lett.* **125**, 168001 (2020).
- [21] E. F. Keller and L. A. Segel, *J. Theor. Biol.* **26**, 399 (1970).
- [22] E. F. Keller and L. A. Segel, *J. Theor. Biol.* **30**, 225 (1971).
- [23] B. Liebchen, D. Marenduzzo, I. Pagonabarraga, and M. E. Cates, *Phys. Rev. Lett.* **115**, 258301 (2015).
- [24] B. Liebchen, D. Marenduzzo, and M. E. Cates, *Phys. Rev. Lett.* **118**, 268001 (2017).
- [25] H. Zhao, A. Košmrlj, and S. S. Datta, *Phys. Rev. Lett.* **131**, 118301 (2023).
- [26] J. R. Howse, R. A. L. Jones, A. J. Ryan, T. Gough, R. Vafabakhsh, and R. Golestanian, *Phys. Rev. Lett.* **99**, 048102 (2007).
- [27] D. T. Chen, M. Heymann, S. Fraden, D. Nicastro, and Z. Dogic, *Biophys. J.* **109**, 2562 (2015).
- [28] The chemokinetic effect directly captured by this model is called *orthokinesis*. We note that there is also *klinokinesis*, which couples D_r to the chemical concentration. While the distinction between these two is important in the biological context, they are not fundamentally different in the physical context since a klinokinetic system can be mapped to an orthokinetic system by suitable rescaling of time. Thus, here we focus only on the latter.
- [29] J. Videler and B. Nolet, *Comp. Biochem. Physiol. A* **97**, 91 (1990).
- [30] J. Ohlberger, G. Staaks, and F. Hölder, *J. Comp. Physiol. B* **177**, 905 (2007).
- [31] T. Vicsek, A. Czirók, E. Ben-Jacob, I. Cohen, and O. Shochet, *Phys. Rev. Lett.* **75**, 1226 (1995).
- [32] S. Saha, J. Agudo-Canalejo, and R. Golestanian, *Phys. Rev. X* **10**, 041009 (2020).
- [33] G. Pisegna, S. Saha, and R. Golestanian, “Emergent polar order in non-polar mixtures with non-reciprocal interactions,” [arXiv:2404.05396 \[cond-mat.soft\]](https://arxiv.org/abs/2404.05396).